Proton Environment of Reduced Rieske Iron−Sulfur Cluster Probed by Two-Dimensional ESEEM Spectroscopy

Derrick R. J. Kolling,[⊥,†] Rimma I. Samoilova,[‡,||] Alexander A. Shubin,[§] Antony R. Crofts,*[,†,||] and Sergei A. Dikanov*[,⊥]

Center for Biophysics and Computational Biology, University of Illinois, Urbana, Illinois 61801, Institute of Chemical Kinetics and Combustion, Russian Academy of Sciences, Novosibirsk 630090, Russia, Boreskov Institute of Catalysis, Russian Academy of Sciences, Novosibirsk 6300090, Russia, Department of Biochemistry, University of Illinois, Urbana, Illinois 61801, and Department of Veterinary Clinical Medicine, University of Illinois, Urbana, Illinois 61801

Received: July 30, 2008; Revised Manuscript Received: October 17, 2008

The proton environment of the reduced [2Fe-2S] cluster in the water-soluble head domain of the Rieske iron−sulfur protein (ISF) from the cytochrome bc_1 complex of *Rhodobacter sphaeroides* has been studied by orientation-selected X-band 2D ESEEM. The 2D spectra show multiple cross-peaks from protons, with considerable overlap. Samples in which ^1H_2O water was replaced by ^2H_2O were used to determine which of the observed peaks belong to exchangeable protons, likely involved in hydrogen bonds in the neighborhood of the cluster. By correlating the cross-peaks from 2D spectra recorded at different parts of the EPR spectrum, lines from nine distinct proton signals were identified. Assignment of the proton signals was based on a point-dipole model for interaction with electrons of Fe(III) and Fe(II) ions, using the high-resolution structure of ISF from *Rb. sphaeroides*. Analysis of experimental and calculated tensors has led us to conclude that even 2D spectra do not completely resolve all contributions from nearby protons. Particularly, the seven resolved signals from nonexchangeable protons could be produced by at least 13 protons. The contributions from exchangeable protons were resolved by difference spectra (^1H_2O minus ^2H_2O), and assigned to two groups of protons with distinct anisotropic hyperfine values. The largest measured coupling exceeded any calculated value. This discrepancy could result from limitations of the point dipole approximation in dealing with the distribution of spin density over the sulfur atoms of the cluster and the cysteine ligands, or from differences between the structure in solution and the crystallographic structure. The approach demonstrated here provides a paradigm for a wide range of studies in which hydrogen-bonding interactions with metallic centers has a crucial role in understanding the function.

Introduction

The bc_1 complex family of proteins carries some 30% of the flux of energy through the biosphere, and has been studied in the context of its role in respiration and bacterial photosynthesis, or (as the b_6f complex) in the oxygenic photosynthesis of cyanobacteria and green plants. All systems function by using a modified Q-cycle, conveniently studied in the bc_1 complex of photosynthetic bacteria such as *Rhodobacter sphaeroides*.[1,2] The rate-limiting step in normal turnover is the so-called bifurcated reaction at the ubihydroquinone (quinol, QH_2) oxidizing Q_o-site.[3−7] The first electron from quinol is passed via the Rieske iron−sulfur protein (ISP) to heme c_1 (the redox center of cytochrome (cyt) c_1), and then cyt *c*, forming a high-potential chain leading to the terminal oxidant (the oxidized photochemical reaction center). The intermediate semiquinone left at the Q_o-site is oxidized by a lower potential chain of heme b_L and heme b_H in the cyt *b* subunit, which passes the electron to the Q_i-site,[8,9] at which ubiquinone is reduced to QH_2 on two successive turnovers of the Q_o-site.

Several critical features of the reaction at the Q_o-site are determined by the properties of the ISP. Structures available from the mitochondrial complexes[6,10−13] had suggested a mobility of the extrinsic head domain of ISP, involving a rotational displacement over a distance of ∼25 Å that positioned the cluster close to either its electron donor or acceptor, so as to facilitate electron transfer through the distance separating these two sites. The mobile domain acts effectively as a bound substrate, forming enzyme substrate (ES)-complexes at the interface on cyt *b* where it reacts with QH_2, and at an interface with cyt c_1 and its heme, which is the electron acceptor. The physiological properties that determine properties of the ES-complex with QH_2 controlling the limiting reaction are the redox potential of the [2Fe-2S] cluster (the acceptor of the first electron) and the p*K* of one of the histidine side chains that acts as a ligand to the cluster. This group also forms a hydrogen bond with the QH_2 to form the ES-complex at the Q_o-site. The importance of this step can only be fully appreciated in the context of the thermodynamic landscape of the modified Q-cycle,[2] minimization of "short circuits" through the Q_o-site,[16−18] and optimization of productive forward chemistry.[3,19] The importance of redox matching is clear from the "tuning" of E_m of the cluster to

* To whom correspondence may be addressed. E-mail: a-crofts@life.uiuc.edu and dikanov@illinois.edu.
⊥ Present address: Department of Chemistry, Princeton University, Princeton, NJ 08540.
† Center for Biophysics and Computational Biology, University of Illinois.
‡ Institute of Chemical Kinetics and Combustion, Russian Academy of Sciences.
|| Department of Biochemistry, University of Illinois.
§ Boreskov Institute of Catalysis, Russian Academy of Sciences.
⊥ Department of Veterinary Clinical Medicine, University of Illinois.

10.1021/jp806789x CCC: $40.75
Published on Web 12/18/2008

compensate for the different redox potentials of its respective partners: the quinol and acceptor components in the high potential chain.[20,21] The element(s) responsible for this tuning are therefore of major interest. The thermodynamic properties are determined by the protein structure in the cluster environment.[5,14−17] Several different hypotheses have been proposed: solvent accessibility to the cluster, the electronic environment of the cluster, electron-withdrawing effects of H-bond donors, and cluster geometry.[22−25]

In addition to the intrinsic properties, the interaction energy for formation of its various complexes also modifies the measured potential of the cluster.[26−28] The $g_x = 1.8$ signal, seen in continuous-wave (CW) EPR spectra of bc_1 complexes, has been interpreted as an indicator of the enzyme−product complex between reduced ISP and quinone; changes in the signal position and width in the presence of other Q_o-site occupants and short-chain alcohols have been used diagnostically in discussions of mechanism.[27,28,31−37] High-resolution EPR studies have provided direct evidence of the enzyme−product complex between reduced ISP and quinol,[38] but interpretation of the $g_x = 1.8$ signal in terms of the **g**-tensor is still speculative,[39] although some progress has been made in mapping the **g**-tensor of the reduced cluster.[27,40] The physical basis of these effects will depend on the nature and the strength of intermolecular interactions, and the way in which they change the electronic structure of the cluster, thus altering its EPR spectra and other properties. Because of their static nature, crystal structures of bc_1 complexes can reveal only limited information pertinent to analysis of these configurational effects,[29,30] but high-resolution EPR can provide both distance and orientation for H-bonds, and is thus a convenient method for extending structural studies.

To take fuller advantage of these approaches, it is necessary first to characterize the intrinsic environment of the cluster. The high quality of data needed demands high sample concentrations, and to achieve these we have used proteolytic cleavage of the head domain of ISP to give a soluble fragment. This has provided a model system that can also be used for crystallography, other spectroscopies, and in comparative studies using soluble Rieske-type proteins from bacteria. Further work based on advanced EPR approaches could help to correlate changes in electronic structure of the reduced cluster accompanying structural reorganization of its protein environment.

Our previous experiments exploiting 2D ESEEM spectroscopy (HYSCORE) have provided information about unpaired spin density transferred on the liganding histidines and noncoordinating nitrogens around the Rieske [2Fe-2S] center in archaeal protein, sulredoxin, and ISP,[41−43] and shown changes in the deprotonation of the noncoordinating imidazole nitrogen in histidine ligands.[44]

In the work reported here, we have used 2D ESEEM spectroscopy and isotopic exchange with ^2H_2O to characterize the proton environment of the reduced Rieske cluster in ISP. We have determined the magnetic and structural characteristics of protons in cysteine and histidine ligands, and protons contributing to hydrogen bonds that determine the physicochemical properties of the cluster. This is the first such attempt to obtain detailed information about the proton environment with use of frozen protein solutions, and our results provide new knowledge about the Rieske cluster that complements the information available from crystallographic, NMR, and ENDOR structural studies. The high-resolution structures of ISP now available allow us to test the structural conclusions derived from the pulsed EPR data, and to establish the phenomenological relationship between structural and magnetic characteristics of the protons, which can be used in future studies devoted to an atomic level understanding of intermediate reaction states.

Experimental Methods

Sample Preparation. Growth of *Rb. sphaeroides*, purification of the bc_1 complex, and isolation of ISF (ISP, with a cleaved N-terminus) were performed as previously described.[45] Protein that was ^{15}N-labeled was prepared by growing *Rb. sphaeroides* in $^{15}N/^{14}N$-exchanged Sistrom media as described in ref 43. The working buffer used for all ISF samples was 50 mM KH_2PO_4, pH 7.0, 400 mM NaCl, and 20% (v/v) glycerol (as a cryoprotectant). We found no evidence that freezing of samples in this medium had any deleterious effect (see the Supporting Information). The working buffer used for bc_1 samples was 50 mM MOPS, pH 7.8, 100 mM NaCl, 1 mM $MgSO_4$, 0.01% *n*-decyl-β-D-maltoside (w/v), and 15 μg/mL phosphatidyl choline (Avanti Polar-Lipids, Inc., Alabaster, AL). Samples were reduced with buffered (50 mM MOPS, pH 7.0) sodium ascorbate and placed into a quartz cuvette (Wilmad-Labglass, Bueno, NJ) with Teflon tubing to prevent scratching. The ^{15}N-labeled samples were frozen slowly directly in liquid nitrogen (this method was sufficient to form a glass as determined by comparison with samples that had been flash frozen with a 1:5 methylcyclohexane:isopentane mixture chilled to almost 77 K).

EPR Spectroscopy. The CW-EPR measurements were made on a Varian (Palo Alto, CA) E-112 X-band spectrometer fitted with an Air Products (Allentown, PA) variable temperature cryostat and a Varian TE_{102} mode cavity. Parameters of individual experiments are reported in the figure legends. The ESEEM measurements were made with an ELEXSYS E580 X-band spectrometer (Bruker, Billerica, MA) with an Oxford CF 935 cryostat. Several types of electron spin echo (ESE) measurements with different pulse sequences were employed, with appropriate phase-cycling schemes used to eliminate unwanted features from experimental echo envelopes. Among them were two-pulse sequences and one- and two-dimensional three- and four-pulse sequences. In the two-pulse sequence ($\pi/2-\tau-\pi-\tau-$echo), the intensity of the echo signal at a fixed interval, τ, between the two microwave pulses with spin vector rotation angles $\pi/2$ and π, is measured as a function of magnetic field. This type of measurement performed at constant τ and varying field is termed a "field-sweep", and at settings at which modulation from magnetic nuclei are minimized (long pulse lengths, $\pi \geq 100$ ns), the EPR spectrum obtained by plotting the echo against field strength is comparable to the integral of the derivative spectrum collected by CW-EPR. In the two-dimensional four-pulse experiment ($\pi/2-\tau-\pi/2-t_1-\pi-t_2-\pi/2-\tau-$echo) known as HYSCORE,[46] the intensity of the inverted echo after the fourth pulse was measured with varied t_1 and t_2 and constant τ. Such a two-dimensional set of echo envelopes gives, after complex Fourier transformation, a two-dimensional spectrum with equal resolution in each direction. HYSCORE spectra vary as a function of the magnetic field and the time, τ, between first and second pulses. The spectra were therefore measured at several τ values at each magnetic field. Parameters of individual experiments are reported in the figure legends.

Spectral processing of ESEEM patterns was performed with WIN-EPR software (Bruker). Processing first consisted of subtracting the monotonic component of the decay from time traces (real and imaginary parts) by a two- to sixth-order polynomial to remove the echo decay function. The time trace was then zero-filled to double the number of points over that collected. Following this, a Hamming window function was applied and the magnitude Fourier spectra were calculated.

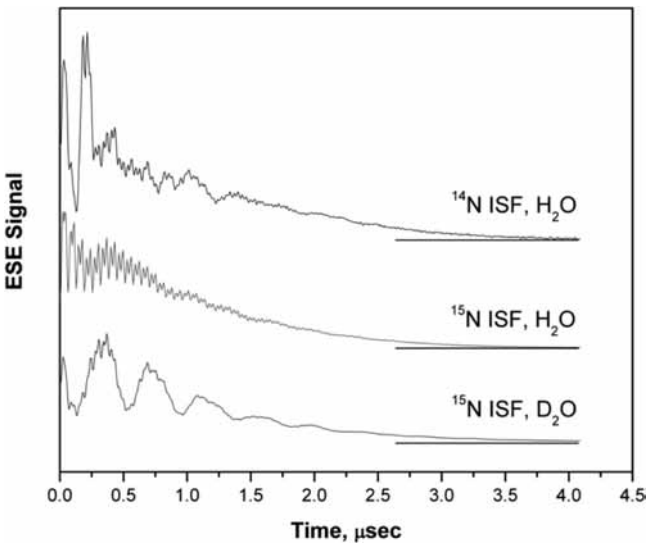

Figure 1. Typical two-pulse echo envelopes of the reduced Rieske cluster of ISF: (a, top) in protein with natural abundance of magnetic nuclei in ^1H_2O buffer; (b, middle) using ^{15}N-labeled ISF in ^1H_2O buffer; and (c, bottom) using ^{15}N-labeled protein in ^2H_2O buffer. All traces were recorded by using a magnetic field giving the maximum EPR intensity corresponding to the intermediate principal value g_y.

Aspects of HYSCORE spectra from $I = {}^1/_2$ nuclei[46,47] of importance for this work, and characteristic spectra from this study are described in the Supporting Information.

Results

EPR and ESEEM of ISF. The EPR spectrum of reduced ISF is an anisotropic line with a width of ~50 mT corresponding to a rhombic **g**-tensor with principal values $g_{z,y,x} = 2.028, 1.898, 1.760$ (see, Figure 2), which are consistent with those previously reported.[22] In Figure 1, two-pulse echo envelopes of the relaxation of the electron spin population of the reduced Rieske cluster of ISF are shown. Samples were prepared as follows: (a) for protein with magnetic nuclei at natural abundance, in H_2O buffer, (b) for ^{15}N-labeled ISF in ^1H_2O buffer, and (c) in ^{15}N-labeled protein in ^2H_2O buffer. The patterns were recorded at the same field position, with the maximum EPR intensity corresponding to the intermediate principal value g_y of the **g**-tensor. The echo envelope in Figure 1a shows deep periodic variations of amplitude, mainly produced by interaction of the electron spin with ^{14}N nuclei of coordinated N_δ from histidine ligands.[38,42,48−51] This feature disappeared after the replacement of the ^{14}N (nuclear spin $I = 1$) by ^{15}N ($I = {}^1/_2$) nuclei (Figure 1b). The ^{15}N nucleus has different magnetic characteristics, including the absence of a nuclear quadrupole moment, and produces a modulation of the echo amplitude that is shallower than that of the ^{14}N isotope. In addition, the spectrum of this sample clearly reveals the presence of periodic variations of high frequency from protons in the local environment of the [2Fe-2S] cluster. Deuterium exchange is accompanied by the appearance of a deep modulation with frequency ~2 MHz from deuterium nuclei that replaced the exchangeable and solvent protons around the cluster (Figure 1c). Analysis of the 1D- and 2D-ESEEM spectra of reduced Rieske clusters from ^{14}N and ^{15}N nuclei has been previously performed[38,41−44,48−51] and is not in the scope of the present work.

HYSCORE Spectra. To obtain quantitative information about the proton environment, we performed HYSCORE experiments, because the simpler 1D approaches do not provide the necessary resolution among multinuclear contributions from protons. HYSCORE spectroscopy makes it possible to deconvolute overlapping peaks that are present in 1D spectra by spreading information out into 2D, where hyperfine (HF) coupling is visualized in the form of off-diagonal cross-peaks. In our studies of protons we used uniformly ^{15}N-labeled protein. This is because the coordinating $^{14}N_\delta$s of histidine ligands produce deep ESEEM that significantly suppresses proton peaks in HYSCORE spectra due to cross-suppression effect. The ESEEM depth from ^{15}N nuclei is considerably smaller, which improves the intensity and resolution of the proton spectra. This phenomenon was recently described in greater detail by Stoll et al.[52] Cross-suppression effects in the HYSCORE spectra of ISF arising from ^{15}N and ^{2}H (appearing after ^{1}H/^{2}H exchange) are more fully described in the Supporting Information. Our analysis allows us to conclude that these have only a weak influence on differences in the proton part of the spectra before and after ^{1}H/ ^{2}H exchange.

Nonexchangeable Protons. HYSCORE spectra were measured at different magnetic fields in the anisotropic EPR line to select different orientations of the effective **g**-tensor (and cluster) relative to the magnetic field direction. Figure 2 (and the Supporting Information) shows representative orientation-selected HYSCORE spectra, in stacked and contour presentation, from nonexchangeable protons in the reduced ISF after ^{1}H/^{2}H exchange. The ^2H_2O-exchange has uncovered peaks that previously had been obscured by the solvent-exchangeable protons. Each spectrum contains multiple cross-peaks. The number of cross-peaks, their intensity, and their location vary as a function of the magnetic field and time, τ.

A method based on a full set of HYSCORE spectra has previously been developed to correlate the peaks from different protons, and to extract their HF tensors.[53] The contour line shape (the ridge forming each cross-peak on a contour plot) for an $I = {}^1/_2$ nucleus coupled to an electron spin $S = {}^1/_2$ by an axial HF interaction in an orientation-disordered sample (corresponding to frozen protein solution) is described by eq 1:[54]

$$\nu_\alpha{}^2 = Q_\alpha \nu_\beta{}^2 + G_\alpha \quad (1)$$

where $Q_\alpha = (T + 2a - 4\nu_I)/(T + 2a + 4\nu_I)$ and $G_\alpha = [2\nu_I(4\nu_I{}^2 - a^2 + 2T^2 - aT)]/(T + 2a + 4\nu_I)$, and a, T are defined in Table 1, and ν_I is the Zeeman frequency. When plotted in the coordinates $\nu_\alpha{}^2$ vs. $\nu_\beta{}^2$, the contour line shape is transformed into a straight-line segment whose slope and intercept are give by Q_α and G_α. A simple extrapolation of the straight line permits the determination of a and T.

For comparison of data from HYSCORE spectra obtained at different field positions, the frequencies of cross-peaks must be recalculated for a common proton Zeeman frequency ν_I. The two frequencies from a spin $I = {}^1/_2$ in the α and β electron spin manifolds can always be written for arbitrary Zeeman frequency, ν_I' and orientation in the general form[55]

$$\nu_{\alpha(\beta)} = \left[\left(\nu_I' + (-)\frac{A}{2}\right)^2 + \frac{B^2}{4}\right]^{1/2} \quad (2)$$

The secular, A, and nonsecular, B, parts of the hyperfine interaction for any pair of frequencies ν_α and ν_β are derived from eq 2 as

$$A = \frac{\nu_\alpha^2 - \nu_\beta^2}{2\nu_I'}$$
$$B^2 = 2\left[\nu_\alpha^2 + \nu_\beta^2 - 2\nu_I'^2 - \frac{(\nu_\alpha^2 - \nu_\beta^2)}{8\nu_I'^2}\right] \quad (3)$$

These values of A and B^2 can be used with eq 2 to calculate ν_α and ν_β corresponding to a different ν_I and magnetic field.

The coordinates of selected points along the ridge of the proton cross-peaks were measured from all available HYSCORE spectra. These sets of points were recalculated to a common Zeeman frequency, arbitrarily selected as ν_I=15.115 MHz (at a magnetic field 355 mT), using eqs 2 and 3 and were plotted in the coordinates ν_α^2 vs. ν_β^2 (Figure 3). The larger frequency of each pair was arbitrarily assigned as ν_α, and the smaller as ν_β. In such a representation, all points fell along seven straight lines 1−7 with the slopes and intercepts shown in Table 1, which were used to calculate two possible sets of (a,T) that satisfy eq 1. Selection of the correct set from the two evaluated here cannot be based solely on the HYSCORE spectra because the lines in these spectra have zero intensity in the canonical orientations of the HF tensor. Tentative assignments were made by using approaches justified in the Discussion section.

One caveat is necessary here. The approach described for determination of HF tensors based on recalculation of the ^{1}H nuclear frequencies measured at different positions of the EPR line shape ignores the influence of **g**-tensor anisotropy. To test for such effects we simulated orientation-selected HYSCORE spectra for the range of parameters shown in Table 1 for the **g**-tensor anisotropy of the reduced Rieske cluster indicated above, and for different relative orientations of **g** and HF tensors. These tests have shown that the set of a and T values determined from the analysis of simulated spectra, using the procedure applied to experimental spectra, deviates <5% from the values of a and T used for the spectral simulations. Thus, **g**-tensor anisotropy has a minimal influence on a and T values summarized in Table 1. On the other hand, in neglecting this dependence, we lose the information about relative orientation of the **g** and HF tensor which could ultimately lead to assignment of different signals to particular protons. However, at this stage of our study, in the context of the very crowded 2D spectra observed for this protein, we must be satisfied with achieving the simpler aim of identifying a maximal possible number of proton signals, and considering their possible assignment qualitatively.

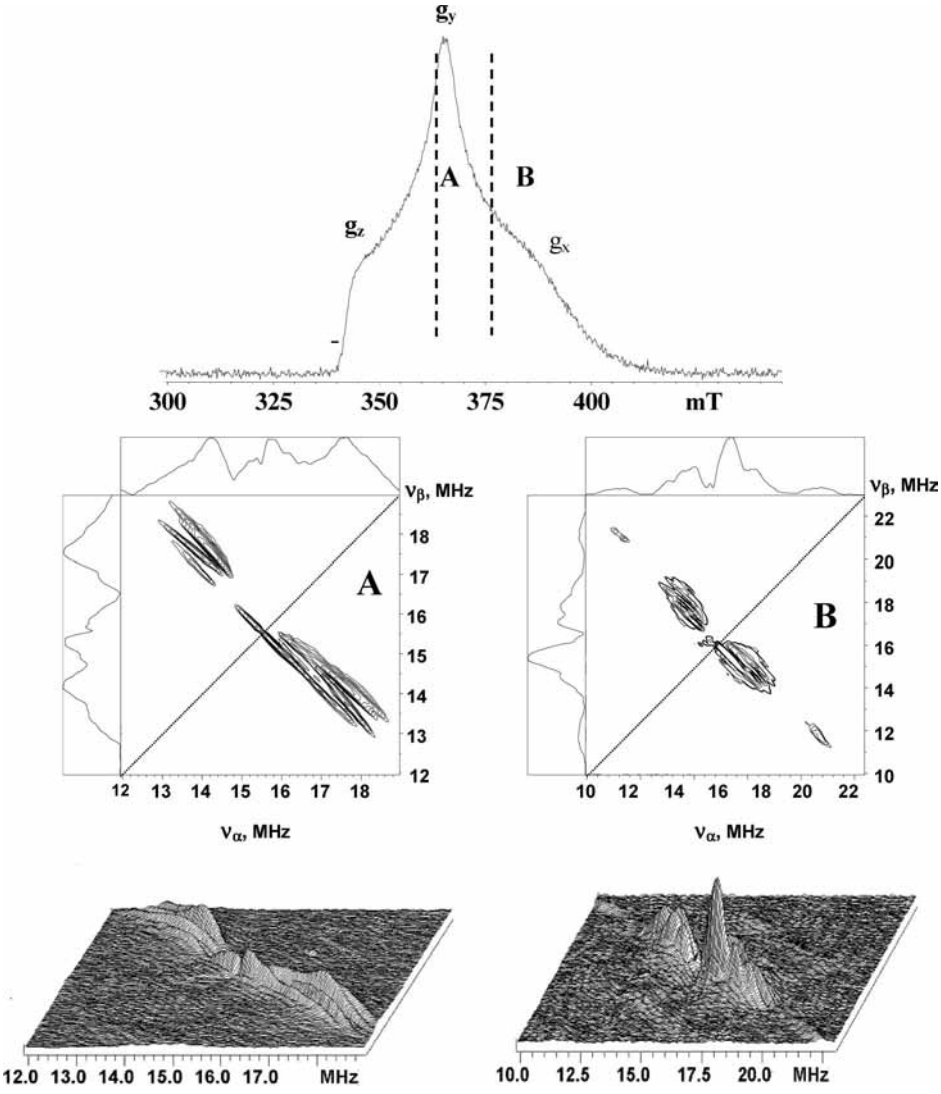

Figure 2. Representative contour plots (middle) and stacked presentations (bottom) of ^{1}H HYSCORE spectra of ^{15}N ISF in ^2H_2O. The spectra show the cross-peaks produced by the nonexchangeable protons located in the neighborhood of the cluster. The spectra are obtained with the time between first and second microwave pulses τ = 240 ns; magnetic field, 363.8 (A) and 375.8 mT (B) (see 2-pulse field-sweep EPR spectrum, top). Measurements were made with a microwave frequency ~9.7 GHz at 10 K.

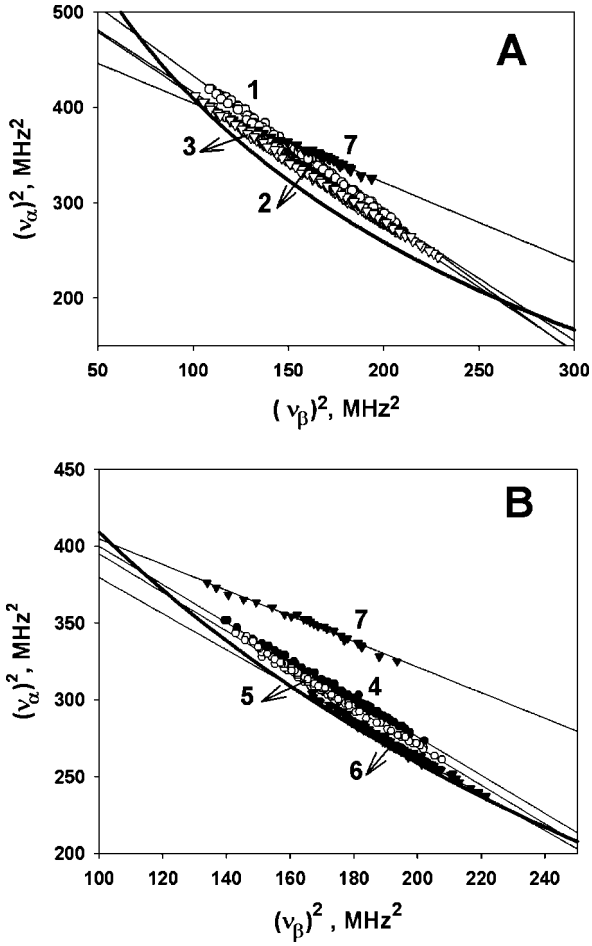

Figure 3. Coordinates of points from the ridges of cross-peaks from nonexchangeable protons observed in HYSCORE spectra measured at several fields across the EPR spectrum for different τ values and referenced to a common $\nu_I = 15.115$ MHz and plotted as sets of values for ν_α^2 versus ν_β^2. All points shown fell along seven straight lines (graph (A)—1(○), 2 (●), 3 (▽), 4 (▼); graph (B)—5(●), 6(○), 7(▼)) indicating seven different protons. The points have been fitted by linear regression to give the slopes and intercepts shown in Table 1. The heavy curve in A and B is defined by $|\nu_\alpha + \nu_\beta| = 2\nu_I$ (using $\nu_I = 15.115$ MHz).

TABLE 1: Characteristics of the Nonexchangeable Proton Signals Derived from HYSCORE Spectra of the Reduced Rieske Cluster in ISF[a]

proton	Q_α	G_α, MHz^2	a, MHz	T, MHz	T_{max}, MHz
1	−1.45 (0.01)	578.2 (1.1)	−8.15; 2.93	5.22	10.44
2	−1.30 (0.01)	546.8 (1.7)	−6.36; 1.52	4.84	9.68
3	−1.34 (0.004)	546.0 (0.6)	−6.46; 2.26	4.20	8.40
4	−1.24 (0.01)	524.3 (1.6)	−5.16; 1.4	3.76	6.52
5	−1.26 (0.01)	520.8 (1.7)	−5.00; 1.91	3.06	6.12
6	−1.18 (0.01)	497.3 (1.9)	−3.27; 1.64	1.64	3.28
7	−0.83 (0.02)	488.3 (3.4)	−1.50; −6.90	8.40	16.80

[a] Coefficients Q_α and G_α are described in eq 1 of the text; a is the isotropic hyperfine coupling; T is the anisotropic perpendicular component of HF tensor defined as $(a - T, a - T, a + 2T)$; $T_{max} = 2T$.

Exchangeable Protons. Samples in ^2H_2O buffer were compared with those in ^1H_2O to identify solvent-exchangeable protons. A large number of nonexchangeable protons with similar nuclear frequencies produced closely located and sometimes even partially overlapping cross-peaks (Figures 2 and SI). The difficulties in deconvolution of peaks of exchangeable protons arising from overlap is compounded by the fact that loss of a peak in a background of nonexchangeable protons of strong intensity may appear simply as a distortion of the shapes of cross-peaks seen in the stacked presentation. However, this would not appreciably affect the cross-peak contour.

Cross-peaks with dominating contributions from solvent-exchangeable protons were resolved at several magnetic fields and τ values (Figures 4 and SI). In the samples prepared in ^1H_2O and in ^2H_2O and measured at the same magnetic fields and τ values, the ratio of the peak intensities from weakly and strongly coupled ^{15}N atoms in the (+,+) and (+,−) quadrants remains the same within 5−10% (Figure S1, Supporting Information). This result provides support for the conclusion that the cross-suppression effect from the intense deuterium signal in the sample with ^2H_2O is weak, and that the changes observed in the proton spectra after deuterium exchange resulted mainly from the replacement of exchangeable protons. It also provides a means for normalization of the 2D spectra, allowing us to resolve contributions from exchangeable protons buried within multiple peaks by creating difference spectra between the sample in ^1H_2O and in ^2H_2O, using the peak intensities in the (+,−) quadrant from coordinated $^{15}N_\delta$ of histidine ligands. Representative difference spectra, obtained from subtraction of spectra shown in Figure S1 in the Supporting Information, are provided in Figure 4.

The coordinates of the cross-peaks obtained in the difference spectra were also recalculated to the same Zeeman frequency (15.115 MHz) and plotted in ν_α^2 vs. ν_β^2 coordinates. The plotted points fell along three straight lines 8, 9, and 9′ (Figure 5 and Table 2), initially interpreted as resolution of three types of exchangeable protons (as mentioned previously, the larger frequency of each point was arbitrarily selected as ν_α, and the smaller as ν_β for all cross-peaks). However, we found in such a presentation that the slopes of the linear regression for the 9 and 9′ peaks have an inverse relationship, i.e. $Q_\alpha(2) \cong 1/Q_\alpha(2')$. This means that the 9′ peak is produced by the same proton, but belongs to the cross-feature with opposite assignment of the nuclear frequencies, i.e. $(\nu_\beta > \nu_\alpha)$ instead of $(\nu_\alpha > \nu_\beta)$.[54,56] In other words, 9 and 9′ are parts of the same cross-feature located on different sides relative to the diagonal of the spectrum. Figure 5 shows the plot where the smaller coordinates for cross-peak 9′ were assigned to ν_α and larger ones to ν_β. In such a presentation, the points from 9 and 9′ fit the linear regression well, thus justifying their possible assignment to one proton. The characteristics of the slopes and intercepts for the linear regressions shown in Figure 5 are presented in Table 3, together with two possible sets of (a,T) that satisfy eq 1.

Discussion

Relation between Proton Location and Anisotropic Hyperfine Tensor. The Rieske [2Fe-2S] cluster has two iron atoms and two inorganic sulfurs liganded by two histidine imidazolates and two cysteine thiolates. Thus, the nearest environment of the cluster includes four β-protons from the cysteine ligands (Cys-129 and -149), α-protons from the imidazole residues (His-152 and -131), and protons from several other residues not involved in direct iron coordination but suitable for the formation of H-bonds with bridging sulfurs or sulfurs of cysteine ligands. Our structures at 1.2 Å resolution show 18 H-atoms within 3.5 Å of the [2Fe-2S] cluster.[43,57]

Values for the anisotropic HF couplings from protons reflect their location around the cluster. The simplest calculation of the tensor is based on a model of point−dipole interaction of the proton with the electron spins of Fe(III) and Fe(II) ions in the reduced [2Fe-2S] cluster. This approach has previously been

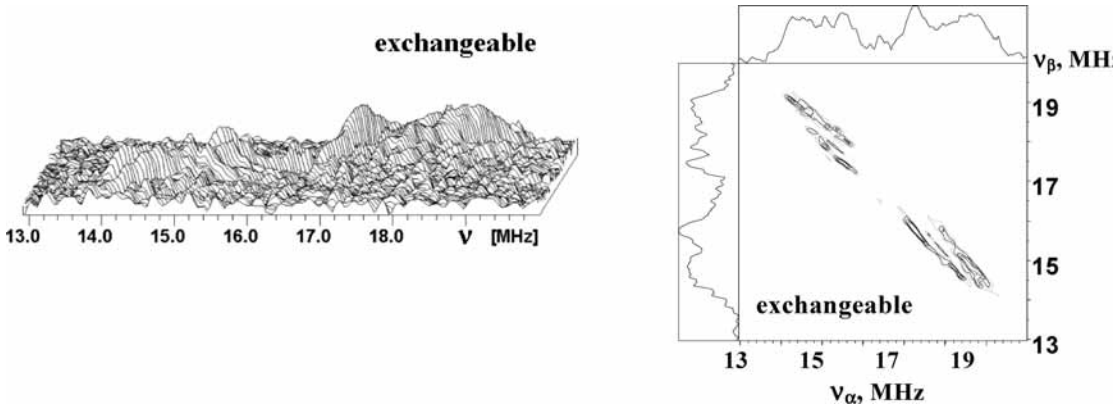

Figure 4. The 3D stacked (left) and contour plots (right) presentations of the lines from exchangeable protons in the HYSCORE spectrum calculated as a difference of the spectra shown in Figure S1 (parts e−h) in the SI.

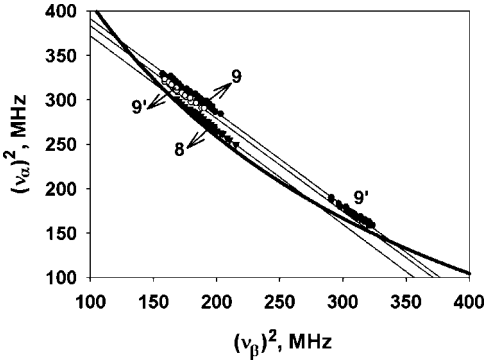

Figure 5. Coordinates of points from the ridges of cross-peaks from exchangeable protons observed in HYSCORE spectra measured at several fields across the EPR spectrum for different τ values and referenced to a common $\nu_I = 15.115$ MHz. Data are plotted as sets of values for ν_α^2 versus ν_β^2. The points have been fitted by linear regression (see details in the text) to give the slopes and intercepts shown in Table 2. The heavy curve is defined by $|\nu_\alpha + \nu_\beta| = 2\nu_I$ (using $\nu_I = 15.115$ MHz).

TABLE 2: Characteristics of the Exchangeable Protons Derived from HYSCORE Spectra of the Reduced Rieske Cluster in ISF[a]

proton	Q_α	G_α, MHz^2	a, MHz	T, MHz	T_{max},[a] MHz
8	−1.06 (0.015)	478.3 (2.8)	−2.19; −0.4	2.60	5.2
9	−0.99 (0.02)	485.0 (3.4)	−2.44; −2.83	5.28	10.56
9′	−1.04 (0.03)	487.9 (5.2)	−2.79; −1.49	4.29	8.58
9 + 9′	−1.05 (0.003)	496.8 (0.7)	−3.24, −1.69	4.94	9.88

[a] See note to Table 1 for description of parameters.

developed by several groups and used for the interpretation of the data obtained from proton ENDOR and ESEEM spectra of Mn(IV)−Mn(III),[58−60] Fe(III)−Fe(II),[61] and Fe(III)−Fe(IV) clusters.[62]

The anisotropic HF tensor of a proton involved in a point−dipole interaction with antiferromagnetically coupled Fe(III) ($S = {}^5/_2$) and Fe(II) ($S = 2$) ions is a sum of the tensors describing the interaction with each ion and including the vector-coupling coefficients determined by the electron spins of the Fe ions

$$\boldsymbol{T}_{dip} = \frac{7}{3}\boldsymbol{T}_{Fe(III)} - \frac{4}{3}\boldsymbol{T}_{Fe(II)} \tag{4}$$

The explicit form of $\boldsymbol{T}_{Fe(III)}$ and $\boldsymbol{T}_{Fe(II)}$ is determined by the location of the proton relative to the Fe(III) and Fe(II). This is characterized by the radial distances Fe(III)−H (r_{III}) and Fe(II)−H (r_{II}) and angles α between (Fe(III)−Fe(II) and Fe(III)−H) and β (Fe(III)−Fe(II) and Fe(II)−H) (Figure 6). The tensors $\boldsymbol{T}_{Fe(III)}$ and $\boldsymbol{T}_{Fe(II)}$ need to be defined in the same coordinate system that introduced the rhombicity into the total dipolar HF interaction, despite the fact that the interaction with each individual ion is axial for point dipoles. General analytical formulas developed by Randall et al.[60] and adapted for the case of the reduced Rieske cluster, Fe(III)−Fe(II), provide the principal values of the resulting dipolar tensor

$$\boldsymbol{T}_{dip} = \begin{bmatrix} \frac{1}{2}\left(\frac{7}{3}T_{III} - \frac{4}{3}T_{II} - 3Z\right) & & \\ & -\left(\frac{7}{3}T_{III} - \frac{4}{3}T_{II}\right) & \\ & & \frac{1}{2}\left(\frac{7}{3}T_{III} - \frac{4}{3}T_{II} + 3Z\right) \end{bmatrix} \tag{5}$$

where

$$Z = \left[\frac{49}{9}T_{III}^2 + \frac{16}{9}T_{II}^2 - \frac{56}{9}T_{III}T_{II}\cos(2\alpha + 2\beta)\right]^{1/2}$$

and $\mathbf{T}_p = (g_e\beta_e g_N\beta_N)/hr_p^3$ (p = III or II) for point dipoles.

The geometric relations between the sides and angles of the triangle allow for definition of the tensor components based on one distance and one angle, for instance r_{III} and β, using the following equations:

$$r_{II} = [r_{III}^2 + r_{II}^2 - 2r_{III}r_{Fe-Fe}\cos\beta]^{1/2}$$
$$\alpha = \arcsin\left[\frac{r_{III}}{r_{II}}\sin\beta\right] \tag{6}$$

These equations allows us to examine the components of HF tensors from the location of the nucleus, defined by r_{III} and β or r_{II} and α.

Figure 7 shows polar graphs (r,φ) with representative contours $T_H = |{}^1/_2({}^7/_3T_{III} - {}^4/_3T_{II})|$ equal to 5.5, 4.4, and 2.5 MHz. In part A, the contours of constant T_H possess a low angular dependence between 180° > φ > 120° when the contour lines deviate very slightly from circles, because the major contribution to the HF tensor is defined by the point−dipole interaction with Fe(III). In addition, the deviation from axiality of the HF tensor defined as $3Z/T_H$ is very low in this angle interval. It is less than 1% for angles 180−150° increasing up to ∼5% at 123°. The tensor rhombicity is progressively increased at smaller φ angles reaching ∼10% at 106° and ∼20% at 90 °. For φ < 60° T_H is held constant by moving closer to Fe(III) because in this region the Fe(II) produces increased dipole field with opposite sign,

TABLE 3: Hyperfine Tensors Calculated in the Point-Dipole Model for the Nonexchangeable and Exchangeable Protons Around the ISF Rieske Cluster[a,b]

Fe(III), residue	atom	r_{III}, Å	φ/β, deg	$\mathbf{T}_{dip}$, MHz	$\lvert T_{max}\rvert$, MHz	$\lvert T'_{max}\rvert$, MHz
Cys-129	HB2 1313	3.21	150/150	(−5.11, −5.0, 10.11)	10.11	7.08
Cys-129	HB3 1314	3.04	121/121	(−6.32, −5.71, 12.03)	12.03	8.42
Cys-149	HB2 1577	3.45	206/154	(−4.06, −4.0, 8.06)	8.06	5.64
Cys-149	HB3 1578	2.95	233/127	(−6.85, −6.36, 13.21)	13.21	9.24
Cys-134	HB2 1380	3.38	105/105	(−4.77, −3.84, 8.61)	8.61	6.0
Ser-154	HB2 1635	3.69	251/109	(−3.54, −2.92, 3.44)	6.46	4.5
Thr-130[c]	H 1322	5.61	116/116	(−0.89, −0.76, 1.65)	1.65	1.17
Gly-133	H 1369	4.72	88/88	(−1.76, −1.07, 2.83)	2.83	1.98
Cys-134	H 1378	4.06	95/95	(−2.79, −1.94, 4.73)	4.73	3.3
Gly-153	H 1624	5.17	76/76	(−1.44, −0.60, 2.04)	2.04	1.42
Ser-154	HG 1637	3.78	279/81	(−4.0, −2.04, 6.08)	6.08	4.25
Ser-154	H 1633	4.40	265/95	(−2.14, −1.48, 3.61)	3.61	2.52
Tyr-156	HH 1676	4.50	234/126	(−1.79, −1.63, 3.42)	3.42	2.39
Fe(II), residue	atom	r_{II}, Å	φ/α, deg	$\boldsymbol{T}_{dip}$, MHz	$\lvert T_{max}\rvert$, MHz	$\lvert T'_{max}\rvert$, MHz
His-131	HB3 1342	2.80	110/70	−12.36, −1.1, 13.46	13.46	9.42
His-131	HE1 1344	3.27	346/166	−4.29, 2.12, 2.17	4.38	3.0
Leu-132	HB2 1356	3.65	74/106	−3.27, 0.78, 2.49	3.27	2.3
Cys-151	HB2 1601	3.38	112/68	−7.26, −1.86, 9.12	9.12	6.39
His-152	HB2 1615	2.86	298/118	−7.29, 2.8, 4.49	7.29	5.1
His-152	HE1 1618	3.24	54/ 126	−4.61, 1.85, 2.77	4.61	3.23
Pro-166	HG2 1823	3.84	78/102	−2.8, 0.5, 2.3	2.8	1.96
Leu-132[c]	H 1354	3.50	104/76	−5.42, −0.74, 6.15	6.15	4.3
His-152	H 1613	3.36	257/ 77	−6.04, −0.53, 6.57	6.57	4.6

[a] r_{III} and r_{II} are distances between proton and Fe(III) and Fe(II), respectively; angles α and β are defined in Figure 6; for protons around Fe(III), $\varphi = \beta$, while for protons around Fe(II), $\varphi = 180° - \alpha$; T_{dip} components of the anisotropic HF tensor calculated in the point-dipole approximation; $|T_{max}|$ is the largest absolute value among the components of $\boldsymbol{T}_{dip}$; $|T'_{max}| = 0.7|T_{max}|$. [b] X-ray data are from PDB file 2NUK. [c] Residues in bold correspond to exchangeable protons.

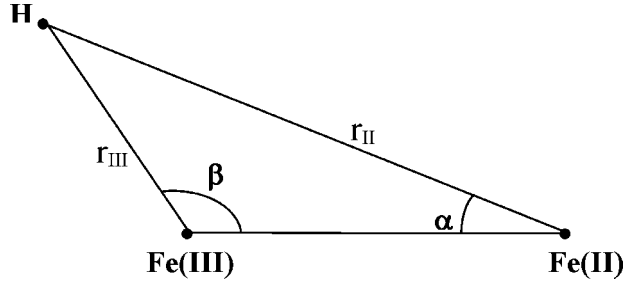

Figure 6. Definition of the distances and angles describing the location of the protons relative to Fe(III) and Fe(II).

which tends to cancel the field from Fe(III). However, this area has no practical interest because it is not accessible for protons.

The contours are axially symmetric about the Fe(III)−Fe(II) line; therefore, the comparison of HF couplings for different protons can be performed by using a single plane defining the location of different protons by r_{III} and β or r_{II} and α. The nonexchangeable and exchangeable protons, located in the region <5 Å from either iron ion, together with r_{III} or r_{II} distances and β or α angles are listed in Table 3, taken from PDB file 2NUK.[57] To visualize the relative location of the protons and corresponding HF couplings, the points with coordinates (r_{III},β) and (r_{II},α) are also plotted on the polar graphs in Figure 7, parts A and B. Relations between φ and α or β angles are described in the caption of Figure 7, and are shown in Table 3. The tensors of the protons calculated by using eqs 4−6 are collected in Table 3 also.

The values calculated by using the point−dipole model suggest that the β-protons of the two cysteine ligands Cys-129 and Cys-149 coordinated to Fe(III) should have HF tensors with the smallest deviation from axial symmetry, and this would suggest the appearance of *single* cross-peaks with sharp ridges from each of these four protons. This is because the major contributions to the anisotropic hyperfine tensor of these protons come from the nearest Fe(III), additionally enhanced by the vector-coupling coefficient ($^7/_3$), which has a magnitude almost two times larger than the coefficient of the remote Fe(II). In contrast, the tensors of the protons located closely to the Fe(II) ion are significantly nonaxial because the contributions of the Fe(II) and Fe(III) ions are comparable in this case, despite the difference in distances. Significant rhombicity of the HF tensor would lead to additional complexity in the spectra because in this case, one proton could produce up to three cross-peaks.[47]

Spin Density Distribution and Valence States. Calculation of the anisotropic HF tensors is performed in the framework of a simple vector-coupling model under the assumption that the unpaired electron spin density in the $S = {}^1/_2$ ground state of the reduced form is fully localized on Fe(III) ($S = {}^5/_2$) and Fe(II) ($S = 2$). However, the detection of the unpaired spin density on nuclei of the surrounding molecules indicates that this is an oversimplified model, and that the delocalization of the spin density from the irons should be considered. The desired spin-population coefficient can be expressed as $D_S(Fe_i) = K(Fe_i)\cdot d_B(Fe_i)$, where $K(Fe_i) = \langle \boldsymbol{S}(Fe_i)\cdot \boldsymbol{S}_{total}\rangle/\langle \boldsymbol{S}^2_{total}\rangle$ is the theoretical vector-coupling coefficient and d_B is a covalency factor, which is the ratio of the spin population of an iron site and the maximum population expected in the valence-bond limit.[63]

Analysis of the ^{57}Fe HF couplings in the major classes of iron−sulfur clusters obtained by Mössbauer and ENDOR spectroscopies[63] has found that a covalency factor d_B is stable and equal to 0.75 for Fe(II) and 0.65 for Fe(III) in reduced [2Fe-2S] clusters with cysteine ligands. This means that instead of a maximal population, which is 4 for Fe(II) and 5 for Fe(III), only about 3 and 3.25 unpaired electrons, respectively, are localized on the irons. Multiplication of these d_B values with

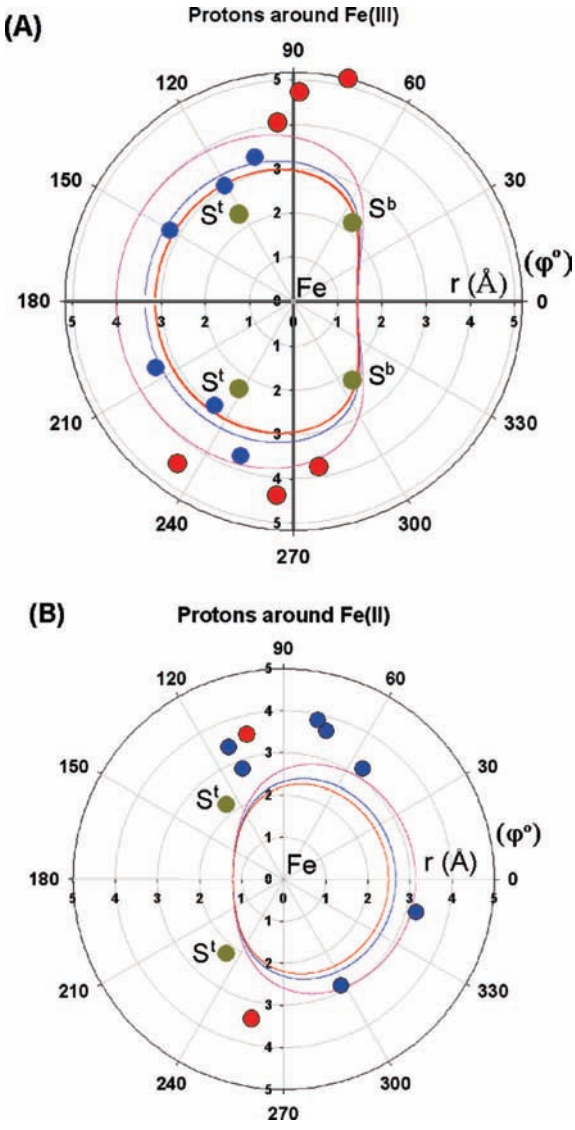

Figure 7. Polar graphs (r,φ) with representative contours $T_H = |^1/_2(^7/_3T_{III} - {}^4/_3T_{II})|$ equal to 5.5, 4.4, and 2.5 MHz around Fe(III) (A) or Fe(II) (B) located at the (0,0) point. For protons around Fe(III), $\varphi = \beta$, while for protons around Fe(II), $\varphi = 180° - \alpha$ (see Figure 6). The blue and red circles correspond to nonexchangeable and exchangeable protons with coordinates shown in Table 3. The gray circles show the positions of bridging and cysteine ligand sulfurs.

vector coupling coefficients ($^7/_3$) for Fe(III) and ($-^4/_3$) for Fe(II) leads to spin population coefficients D_S of ~1.50 for Fe(III) and ~−1.00 for Fe(II). Simulations of experimental orientation-selected proton ENDOR spectra have provided the spin population coefficients $D_S \approx 1.85$ for Fe(III) and $D_S \approx -0.9$ for Fe(II) for [2Fe-2S] cluster in ferredoxin from *A. platensis*.[64] These values were +1.60 and −0.6, respectively, for adrenodoxin and +1.6 and −0.55 for the Rieske cluster in ISF from bovine bc_1 complex.[65] One can note, however, that such significant variations of the D_S should be considered in the light of available data for ^{57}Fe couplings for [2Fe-2S] clusters, which do not show proportional changes of the isotropic HF couplings. Values for Fe(III) and Fe(II) respectively are in ferredoxins (−(47.4−47.9); (21−21.5)) MHz, in adrenodoxin (−49.7, 25.3) MHz, and in Rieske proteins (−49.3; 19.3−20) MHz.[63,66]

Nevertheless, taking into account the covalency factors d_B evaluated for Fe(III) and Fe(II) in reduced [2Fe-2S] cluster[63] one can suggest that the tensors simulated in the point−dipole model are overestimated by a factor 1.3−1.4 ≈ 1/(0.7−0.75). The $|T_{max}| = 2|T_H|$ component of the tensors adjusted according to the covalency factor $d_B \approx 0.7$ is shown in Table 3 as $|T'_{max}|$. Two additional influences can change the actual values of these tensors in comparison with those estimated in the point−dipole model: first is the delocalization of the unpaired spin density on neighbor atoms over chemical bonds, and second is the possible difference of the ligand geometry in the reduced and oxidized states of the cluster, and between the crystallographic and solution structures.

Analysis of the Anisotropic Tensors of Nonexchangeable Protons. The tensors calculated by using the point−dipole approximation provide the simplest basis for an initial qualitative analysis of the experimental data obtained for nonexchangeable and exchangeable protons. The $T_{max} = 2T$ for HYSCORE-characterized proton signals 1−6 are between 10.4 and 3.2 MHz (Table 1). When the influence of the covalency factor is considered, protons with a calculated T_{max} in the range 13.21 and 3 MHz would have adjusted values $|T'_{max}|$ of around 10−2 MHz (Table 3), consistent with those experimentally determined. These include six strongly coupled nonexchangeable protons located near Fe(III) with T_{max} varying from 13.21 to 6.46 MHz. Plausible initial assignments might be to four β-protons from Cys-129 and Cys-149, and two protons from the noncoordinating Cys-134 and Ser-154. The rhombicity of these tensors does not exceed ~10%. Model HYSCORE simulations show that these tensors would still produce cross-peaks consisting of a single line in the spectra. There are also seven nonexchangeable protons from five different residues (see Table 3) near Fe(II) with T_{max} varying over two distinct ranges, between 13.46 and 7.29 MHz and between 4.61 and 2.8 MHz. Their tensors are expected to be strictly rhombic, with nonaxiality up to ~80%. Each proton from this group could produce more than one pair of cross-peaks, thus further complicating the already crowded spectrum by contributions from at least 13 protons (possibly more if complete deuterium exchange did not take place). One can note, however, that the lines produced by these protons may have significantly different intensities; therefore, not all of them would contribute equally to the orientation-selected spectra.

Nonexchangeable protons magnetically coupled to the reduced [2Fe-2S] cluster in plant- and Rieske-type ferredoxins have been identified, and some assigned to specific protons by using paramagnetic NMR,[67−70] ESEEM,[53] and ENDOR.[64,65] To provide some initial reference for the assignment of the observed HF couplings, all available data for proton HF tensors around other reduced [2Fe-2S] cluster with cysteine ligands need to be considered. The ENDOR studies of [2Fe-2S] clusters by orientation-selected ENDOR are particularly relevant to our case.

A detailed orientation-selected ENDOR study of the reduced [2Fe-2S] cluster in *A. platensis* ferredoxin reported the largest principal values to be 9.09, 4.00, 9.7, and 4.08 MHz for the β-protons of the cysteine ligands (Cys-49 and Cys-79) coordinated to Fe(III).[64] The rhombicity of the tensors does not exceed 5%. These protons were identified through correlation between the principal directions of their HF tensors, determined from simulations of largest splittings in ENDOR spectra, and the available crystallographic structures.

On other hand, a 2D-ESEEM study of the reduced [2Fe-2S] cluster in the closely related *Porphira umbilicalis* ferredoxin found only four signals, which were assigned to two groups of β-protons from cysteines coordinated to Fe(II) and Fe(III).[53] The T_{max} of the axial HF tensors determined by applying a procedure similar to the one used in this work yielded 11.2, 8.2, 4.0, and 3.0 MHz. The tensors with T_{max} values of 7.2 and 4.0 or 8.98

and 3.7 MHz were determined for the β-protons from the cysteine ligands coordinated to Fe(III) in adrenodoxin.[65]

The conformations of the cysteine ligands coordinated to either iron in the X-ray structure of *A. platensis* ferredoxin are very similar to each other; this leads to close dihedral angles and Fe−H distances in the two pairs of almost equivalent protons near each Fe. In addition, the structure shows considerable variation of the Fe−H distances for the two protons from the same cysteine ligand, which is close to 1 Å.[71] This is a source of significant difference between the T_{max} magnitudes for these two protons. These peculiarities in the structure actually explain the results of the HYSCORE study.[53] The Fe−H distances for two cysteines near Fe(III) are 3.14 and 3.88 Å, and 2.97 and 4.0 Å in adrenodoxin.[72] However, the structure of *Rb. sphaeroides* ISF[57] (Table 3) shows that the difference in Fe−H distances for the β-protons is much smaller (~0.15 Å in Cys-129 and ~0.5 Å in Cys-149). Similar differences in Fe−H distances for the β-protons of cysteine ligands are reported for the Rieske cluster in the bovine ISF.[73] From this, it is obviously dangerous to attempt any direct extrapolation from analysis of the anisotropic hyperfine tensors based on the large difference seen in ferredoxins and adrenodoxin to the β-protons in ISF.

The first proton ENDOR study of the Rieske ISP from bovine heart mitochondrial cyt bc_1 complex was recently performed by Kappl et al.[65] The smaller spread of Fe−H distances decreases the diversity between the components of the anisotropic HF tensors for β-protons, which resulted in a stronger overlap of the lines in the ENDOR spectra of the Rieske cluster and explains its lower resolution when compared to the spectra of the [2Fe-2S] clusters in ferredoxins. Nevertheless, the HF tensors of five protons assigned to four β-protons from Cys-139 and Cys-158 and one proton from His-141 were reported. The maximal component of the almost axial HF tensors for β-protons of cysteine ligands is ~9.8, 8.4, 6.5, and 5.1 MHz—i.e., the difference between the largest and smallest values is smaller for the Rieske cluster than for the cysteine-ligated systems. The fifth proton, from the C_β of His-141, located between Fe(III) and Fe(II), has a substantially nonaxial tensor with $T_{max} \approx 9.3$ MHz.

Comparing the T_{max} values previously reported for β-protons in cysteine-ligated clusters and Rieske clusters with the values between 10.44 and 3.2 MHz obtained from our analysis for protons 1−6 (Table 1), one can conclude that T_{max} values in the range 10.44 to 6.12 MHz are consistent with ENDOR-derived values, and that four of these tensors may belong to the β-protons of Cys-129 and Cys-149 of the *Rb. sphaeroides* ISF with estimated T'_{max} values of 9.24, 8.42, 7.08, and 5.64 MHz. There are, however, three other protons [HB2 1380 from Cys-134 (near Fe(III)), HB3 1342 from His-131, and HB2 1601 from Cys-151 (both near Fe(II))] with estimated T'_{max} values falling in the same range, and two protons (HB2 1635 from Ser-154 and HB2 1615 from His-152) with estimated T'_{max} that do not differ significantly from the low bound of this interval. The protons near Fe(II) are supposed to possess tensors with significant rhombicity that would effectively decrease the intensity of their signal peaks. Thus, one can suggest that at least some of the resolved peaks do not represent the contribution from individual protons, or that contributions from β-protons dominate the spectra and other protons only slightly affect the peaks from these protons.

The estimated tensors also single out a group of more weakly coupled protons with $T_{max} < 3.3$ MHz. This group consists of one proton near Fe(III) and four near Fe(II). Our data show only one proton signal, **6**, with $T_{max} = 3.06$ MHz. We suggest that the signal includes the unresolved contribution from protons mentioned earlier. Indeed, the examples of the HYSCORE spectra in Figure 3 show that the resolution of the contribution from different protons in 2D spectra is determined by the different deviations of the cross-peak ridges from the line normal to the diagonal at the point where both coordinates are equal to the proton Zeeman frequency. This deviation has a maximum value of the order $\sim 9T^2/32\nu_I$. For $T \approx 5$ MHz, the maximal shift has a value of ~0.5 MHz, but for $T \approx 3$ MHz, this shift has a value ~0.2 MHz. Therefore, when several protons with $T < 3$ MHz contribute to the spectra, their cross-peaks would all be located near the antidiagonal, with deviations less than ~0.2 MHz, and this would preclude resolution of any individual contributions.

TABLE 4: The Principal Values for the Preferred Sets of the Axial Hyperfine Tensors, Which Can Be Assigned to the β-Protons

proton	(a, T), MHz	$A_\perp = a - T$, MHz	$A_\parallel = a + 2T$, MHz
1	2.93, 5.22	−2.29	13.37
2	1.52, 4.84	−3.32	11.2
3	2.26, 4.20	−1.94	10.66
4	1.4, 3.76	−2.36	8.92
5	1.91, 3.06	−1.15	8.03

The orientation-selected HYSCORE spectra have also shown the presence of signal 7 with an effective $T_{max} = 16.8$ MHz obtained from analysis by using an axial approximation. This value for T_{max} considerably exceeds any values estimated by using the point−dipole model. The corresponding cross-peaks, observed in practice in a narrow field interval, possess low intensity. We tentatively assign this signal to a proton with a significantly nonaxial tensor. A possible candidate is the proton HB3 1342 of His-131, which is the proton closest to the iron−sulfur cluster, near the bridging sulfur, a point in space where the point−dipole model would probably not work well, and arguments in support of such an assignment are provided in the Supporting Information.

From the single-crystal and orientation-selected ENDOR data[64,65,74−77] obtained for different proteins we can conclude that of the two possible pairs of HF couplings calculated from the contour line analysis, the isotropic HF coupling of every β-CH_2 proton must have the same sign as the maximal component of the HF tensor ($a + 2T$, $a - T$, $a - T$). This would mean that values for a and T for a β-CH_2 proton have the same sign. This restriction could also be applied for the assignment of our data to particular protons, giving the preferred sets (a, T) for the tensors, together with principal values that can be assigned to the β-protons, shown in Table 4. The $A_\parallel = a + 2T$ values of these tensors determine the maximal splittings, which can be seen in ENDOR spectra. In particular, the maximal width of the ENDOR spectra at ~13−14 MHz of ISF reported by Kappl et al.[65] is consistent with maximal $A_\parallel = 13.37$ MHz from signal 1. Individual couplings of the order ~11 and 9 MHz were also resolved in ENDOR spectra.

Summarizing this discussion, one can conclude that seven resolved signals from nonexchangeable protons represent the contribution from at least 13 protons. From this, at least some of the resolved features must result from the contribution of more than one proton. The resolution achieved by using X-band HYSCORE spectra, together with the methodological approach described here, allows us at this stage to indicate only which groups of protons can contribute to the peaks corresponding to the different values of anisotropic couplings.

TABLE 5: The Parameters of the Functions Describing the Dependence of the Rescaled Isotropic Couplings from the Dihedral Angle

footnote	A	B	C	θ_o	ref
a	−1.52	0.07	2.69	0	75
b	−1.57	−0.4	3.09	0	77
c	3.047	−0.636	−1.174	0	76
d	−0.143	−0.227	1.391	0	76
e	−2.28	0.52	3.03	−21	74

[a] Fit of the rescaled proton HF couplings for CH_2 protons of mixed-valence pair in several oxidized centers I, III, and IV in high potential model compound $[Fe_4S_4]^{3+}$, the data for reduced center $[Fe_4S_4]^{1+}$ do not fit well with this curve.[75] [b] Cluster of *Ectothiorhodospira halophila* iso-II high-potential iron−sulfur protein.[77] [c] Fit of the rescaled proton HF couplings for CH_2 protons of the ferrous, and [d] mixed-valent (b) site in reduced [4Fe-4S]$^{1+}$ model compound.[76] [e] Fit of the rescaled proton HF couplings for CH_2 protons of the ferric and mixed-valent sites in oxidized center IV in high potential model compound $[Fe_4S_4]^{3+}$.[74]

Isotropic Hyperfine Couplings: Dependence on Dihedral Angle. Previous ENDOR investigations proposed that the isotropic hyperfine constant and the paramagnetic shifts of the β-protons in the cysteine ligand of iron−sulfur clusters must depend on the dihedral angle, θ, between the Fe−S−C_β and S−C_β−H planes.[74]

An empirical function of the general type

$$a_{spc} = A\cos^2(\theta + \theta_o) + B\cos(\theta + \theta_o) + C \qquad (7)$$

was used, where A, B, C, and θ_o are parameters determined by fits to experimental data or theory. This function describes the angular dependence for rescaled isotropic HF constants a_{spc}, obtained after the normalization of the experimental proton isotropic constants by the individual spin population coefficients for each individual Fe ion, $a_{spc} = a_{exp}/D_S(Fe_i)$. Therefore, the result would significantly depend on how accurately the $D_S(Fe_i)$ spin populations are determined.

The available examples of the $a_{spc}(\theta)$ function are mostly based on the single-crystal ENDOR data obtained for oxidized and reduced [4Fe-4S] centers in synthetic compounds, which are considered as a model for high-potential iron−sulfur proteins.[74−76] The coefficients of the function $a_{spc}(\theta)$ depend significantly on the particular experimental set used for fitting, which could include the different valence states of the iron, i.e. ferrous Fe^{2+}, mixed-valence $Fe^{2.5+}$, and ferric Fe^{3+}. Examples of these coefficients determined from the fitting of ENDOR-derived proton couplings of [4Fe-4S] centers are shown in Table 5.

In this situation, it would be more reasonable to consider the data available for the -CH_2 protons of groups specifically coordinated to an Fe(III) ion, because this is the ion coordinated by cysteine ligands in the reduced Rieske cluster. The experimental isotropic HF couplings for the β-CH_2 protons coordinated to Fe(III) reported for the different systems are consistent with each other (values reported are 1.6−4.0 MHz in the reduced [2Fe-2S] cluster in ferredoxin from *A. platensis*,[64] 2.3−4.0 MHz in adrenodoxin,[65] and 1.4−4.8 MHz in ISF from bovine heart mitochondria[65]). The isotropic couplings for the -CH_2 protons near the ferric site of the [4Fe-4S] cluster vary within 1−2 MHz.[74] The isotropic couplings determined in our experiments, which can be assigned to the β-protons, are between 1.4 and 2.93 MHz. As noted above, the experimental values of a_{exp} are dependent on the dihedral angle, but their direct comparison requires the correct rescaling. Table 6 includes experimentally determined HF couplings for each particular proton, their rescaled values, and the dihedral angles estimated from the available crystallographic structures. Even a brief analysis of the available data shows that the rescaled isotropic couplings for the close dihedral angles in different samples demonstrate, in some cases, a difference of a factor of ∼2. The best fit of the published data by eq 7 is shown by the solid curve of Figure 8. The shape of this curve suggests that the β-proton closest to Fe(III), HB3 from Cys-149 with dihedral angle $\theta = -33.3°$, should have a smaller isotropic constant than the proton HB3 of Cys-129 with $\theta = -51.3°$. The assignment of the closest proton to the experimental tensor **1** with T_{max}= 10.4 MHz and $a = 2.93$ MHz would not satisfy this requirement, which leads us to the tentative assignment of the tensors **2**−**4** with T_{max}: 9.6, 8.4, 7.5, and 6.1 MHz, and corresponding a_{exp}: 1.59, 2.26, 1.4, and 1.91 MHz to the β-protons of Cys-129 and Cys-149 as shown in Table 6. The isotropic couplings of these protons at corresponding dihedral angles are shown in Figure 8 as filled triangles. The fit of the published data and our data by the dotted curve is also shown in this figure.

Thus, one can conclude that the anisotropic and isotropic couplings of tensors 2−4 fit reasonably well to the reported intervals for the β-protons of cysteine ligands. On the other hand, the large spread of the a_{exp} for the β-protons indicates that at least some of them are determined with significant systematic errors resulting mainly from the complexity of the analyzed spectra and variation of the numerous parameters during the simulation procedures. In our case the signals 2−4 could be affected by contributions from other protons that would influence their contour line shapes and determined HF parameters, respectively.

Exchangeable Protons. Although identification of the non-exchangeable protons is of intrinsic interest, a major practical concern is with the characterization of the exchangeable protons—in particular, the protons involved in hydrogen bond formation with the sulfur bridging atoms and cysteine sulfurs. This is because an approximate correlation has been proposed between the weighted number of hydrogen bonds to the cluster and the redox-potential (E_m) of the Rieske center.[24]

Several groups have reported exchangeable protons in plant and Rieske-type ferredoxin systems using paramagnetic NMR[67−69] and ENDOR.[64,65] Holz et al.[67] identified two solvent-exchangeable HF-shifted protons (one of which took several days to exchange) in a *Xanthobacter* strain Py2 Rieske-type protein, and on this basis, assigned them to the two histidine $N^\varepsilon H$ protons. This assignment, however, was brought into question following isotopic labeling experiments by Xia et al.,[68] who showed that the direction of the chemical shift is not necessarily correlated to the interaction of the proton with either Fe(II) or Fe(III). They identified one readily solvent-exchangeable HF-shifted proton that had an exchange half-time of ∼2 days in the oxidized form (the exchange half-time of the reduced form was undetectable), but were unable to assign it. Interestingly, they found that when growing histidine auxotrophs on a minimal media supplemented with [$^2H^\varepsilon$]His, the $^2H^\varepsilon$ was partially replaced by ^1H through abiotic exchange. However, this phenomenon had a very long half-life, and should not have affected our studies, in which solvent exchange was only carried out over a period of days.

The tentative assignment of some of the exchangeable protons to the two $N^\varepsilon H$, while tempting because they readily exchange protons with the solvent in their oxidized form (pK_a values of 7.6 and 9.6,[23,78] might not be wise, because solvent-exchangeable protons are observed in plant-type ferredoxins that do not have histidine ligands.[69] Other potential candidates for exchange

TABLE 6: Dihedral Angles and Isotropic Hyperfine Couplings Reported for the CH_2 Protons Near Fe(III)

protein	proton	dihedral angle, deg	isotropic coupling (a_{exp}/a_{spc}), MHz	ref
model compound with [4Fe-4S]	1	−43	−1.95/2.7	
	2	80	−1.8/2.5	74
	3	11	−1.04/1.68	
	4	126	−2.00/3.24	
ferredoxin *A. platensis* [2Fe-2S]	Cys-79, HB1	1.7	4.0/2.2	
	Cys-79, HB2	117.7	3.9/2.1	64
	Cys-49, HB1	−2.2	1.6/0.9	
	Cys-49, HB2	116.5	4.1/2.2	
ferredoxin *P. umbilicalis* [2Fe-2S]	Cys-79, HB1	1.7	1.8/1.0	
	Cys-79, HB2	117.7	3.6/1.9	53
	Cys-49, HB1	−2.2	1.8/1.0	
	Cys-49, HB2	116.5	3.6/1.9	
adrenodoxin [2Fe-2S]	Cys-92, HB1	4.6	4.0/2.67	
	Cys-92, HB2	124.6	3.6/2.4	65
	Cys-55, HB1	−18.2	3.2/2.13	
	Cys-55, HB2	101.8	2.3/1.53	
ISF from beef [2Fe-2S] (Set 1)[a]	Cys-158, HB2	89.0	3.1/2.06	
	Cys-158, HB1	−31.1	1.4/0.93	
	Cys-139, HB2	68.3	2.2/1.5	
	Cys-139, HB1	−51.7	4.8/3.2	
ISF from beef [2Fe-2S] (Set 2)	Cys-158, HB2	89.0	4.5/3.0	65
	Cys-158, HB1	−31.0	3.7/2.5	
	Cys-139, HB2	68.3	2.1/1.46	
	Cys-139, HB1	−51.7	2.5/1.67	
ISF from *Rb. sphaeroides* [2Fe-2S]	Cys-129, HB2	67.5	1.4/0.93	this work
	Cys-129, HB3	−51.2	2.26/1.50	
	Cys-149, HB2	86.9	1.19/1.27	
	Cys-149, HB3	−33.3	1.59/1.06	

[a] The fit with Set 1 has a smaller standard error.

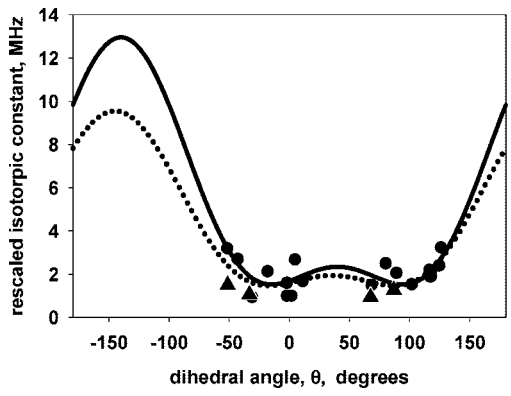

Figure 8. The best fit of the rescaled isotropic HF couplings from the previously published data (filled circles) by eq 7 with the following parameters: $A = 4.59$ MHz, $B = -5.31$ MHz, $C = 3.06$ MHz, and $\theta_o = 40°$ (solid line). The best fit after addition of the couplings (filled triangles) assigned to the β-protons in this work by eq 7 with the following parameters: $A = 3.11$ MHz, $B = -3.8$ MHz, $C = 2.63$ MHz, and $\theta_o = 35°$ (dashed line).

would be the amide backbone protons and protons from side chains within the H-bonding distance of the cluster, Ser-154 and Tyr-156.

ENDOR studies of [2Fe-2S] clusters in ferredoxin and adrenodoxin[64,65] have revealed changes in their spectra after $^1H/^2H$ solvent exchange resulting in intensity variation of some spectral peaks, and interpreted as indicating the overlap of lines from exchangeable and nonexchangeable protons. Simulation of the features produced by exchangeable protons was based on consideration of the -OH and -NH groups with heavy atoms located at distances <4 Å from either of the irons, based on crystallographic structures, and assuming purely HF dipolar interaction with the protons. One can note, however, that the participation of any of these protons in H-bond formation could lead to the appearance of some measurable isotropic coupling due to spin density transfer over the H-bond bridge. ESEEM studies have shown the presence of a peptide nitrogen with isotropic HF coupling up to ~1 MHz near the reduced [2Fe-2S] cluster in ferredoxins and Rieske proteins.[43,79] In addition, the location of the hydrogen atoms involved in H-bond formation could be different in oxidized and reduced proteins and this would be reflected in their HF tensors.

After ^2H_2O-exchange, the [2Fe-2S] cluster showed the appearance of a well-defined echo envelope, with a deuterium frequency at ~2 MHz from nuclei that replaced the exchangeable and solvent protons around the cluster (Figure 1). These interactions contribute to the intense line appearing near the ^2H Zeeman frequency in ESEEM and HYSCORE spectra (see Figure S1 in the Supporting Information). Closely located exchangeable protons involved in stronger interactions with the reduced cluster were visualized in HYSCORE spectra. By subtracting HYSCORE spectra of ^1H_2O- and ^2H_2O-buffered samples, we have revealed the cross-peaks of the exchangeable protons, which can be assigned to two groups (Table 3) with substantially different anisotropic couplings. The protons in one group possess $T_{max} \approx 8-10$ MHz, while T_{max} values are <5 MHz for the protons in the second group. This result shows qualitative correlation with the anisotropic tensors of exchangeable protons calculated in the point−dipole approximation and allows tentative assignment, although some particular values of experimental and calculated tensors are in significant disagreement.

The crystallographic structures show nine potentially exchangeable protons near the cluster, three of which are located within 3.0 Å of the sulfur atoms of the cluster or cysteine sulfurs, distances which might lead to H-bond formation. The tensors calculated for all these protons using the distances from PDB

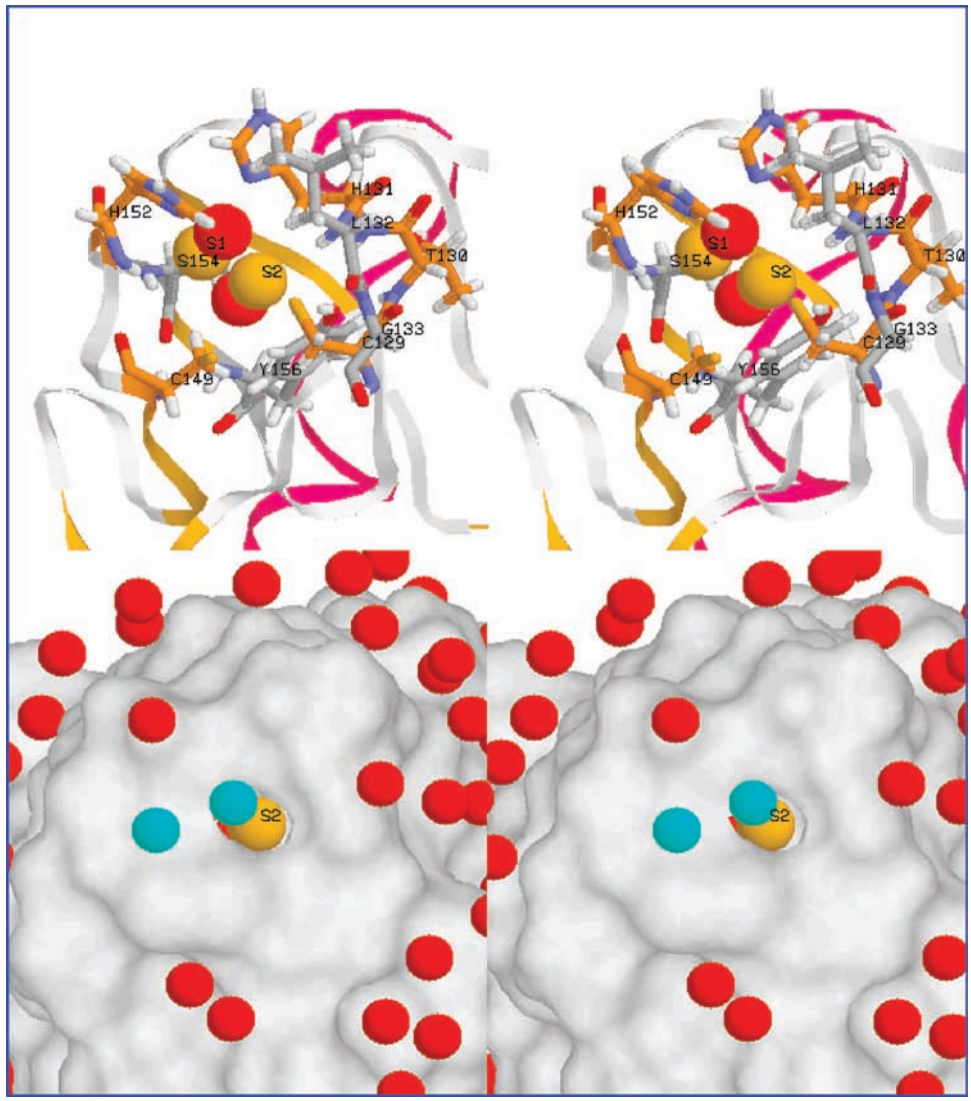

Figure 9. Structure of the Rieske protein in the cluster domain. Top: Cartoon representation of the cluster neighborhood, with residues discussed in the text shown as ball and stick models, colored by atom type. Residues are labeled at their Cα-atoms. The atoms of the cluster are shown as 1.0 Å spheres, with Fe in red, S in yellow. Bottom: The surface of the protein is shown, with crystallographic water molecules shown by their O-atoms. Both waters within 6.0 Å of the cluster are shown in cyan, all others in red. The S2 sulfur of the cluster can be seen through the "window" discussed in the text. (Coordinates from PDB file 2NUK, stereopair for crossed-eye viewing).

file 2NUK (at 1.1 Å resolution) are shown in Table 3. Even the largest calculated value, $T_{max} = 6.08$ MHz for HG1637 from Ser-154, significantly exceeds T_{max} of the other protons in this group, but is considerably smaller than the experimentally determined value of $T_{max} \approx 8-10$ MHz corresponding to the signals 9 and 9′. Two other exchangeable protons, those of H1354 from the peptide -NH of Leu-132, and of H1613 from the peptide -NH of His-152, located near Fe(II), show calculated tensors with similar T_{max} values of 6.15 and 6.57 MHz. One can note that the tensors of these protons are strictly rhombic, and each of these protons could therefore produce more than one ridge, as was discussed for signal 7 in the Supporting Information. Thus, from the point−dipole model, three protons would be expected to have a tensor with $T_{max} \approx 6-6.5$ MHz. All other exchangeable protons located around the cluster have smaller T_{max} values, varying between 1.65 and 4.7 MHz. Considering these results, one can suggest that the signals 9 and 9′ resolved in our spectra are produced by exchangeable protons from Ser-154, Leu-132, and/or His-152. Our earlier studies showed the presence of unpaired spin density producing $a \approx 1$ MHz coupling on a peptide nitrogen, which was identified as that of Leu-132.[43] This result indicates the formation of an H-bond between this nitrogen and the bridging sulfur S2, with a configuration strongly favoring unpaired spin density transfer. Other peptide nitrogens in the protein environment must carry 5 to 10 times less spin density than the peptide N of Leu-132. In line with this result, one can suggest that H1354 of Leu-132 is at least one of the protons possessing the strongest anisotropic HF tensor with $T_{max} \approx 8-10$ MHz. Following the interpretation given for the signals 9 and 9′, we suggest that signal 8 might then represent the unresolved contribution of the remaining more weakly coupled exchangeable protons.

This is the first set of experimental data allowing theoretical calculation of HF tensors for exchangeable protons, and the results must depend on the model used. The discrepancy noted above may indicate either that the point−dipole model failed, or that the location of at least some of the exchangeable protons in the reduced state of cluster is different from the location shown by the crystallographic model. Taking the first possibility, we note that a correct description of the HF tensors requires an adequate accounting for the distribution of electron spin over the cluster and its ligands. Prior result had shown that the

bridging sulfur S2 must carry some unpaired spin density,[80] but we do not yet have a basis for quantitative assignment. The possibilities for geometric inconsistency due to a difference between the solution and the crystallographic structures can only be resolved by additional structural data, but we note that our attempts to generate separate structures for oxidized and reduced samples failed, probably because of radiolytic reduction of the oxidized sample during X-ray illumination,[57] so an explanation in terms of a redox mismatch is unlikely. It is clear that further experimental and theoretical developments as discussed below are needed to obtain more sophisticated characterization of the hydrogen-bonded protons around the iron−sulfur cluster that might throw additional light on their functional importance.

Solvent Access to the Cluster. The HYSCORE spectra obtained under the same conditions in samples prepared in ^1H_2O and ^2H_2O have shown that the contribution of the exchangeable protons to the matrix proton peak (located on the diagonal point around the proton Zeeman frequency) depends on which part of the EPR spectrum was excited. The contribution is minimal for the spectra measured at the edges of the spectrum and grows up to half of the proton peak intensity when measured in the middle of the EPR spectrum. This result could be understood in the light of what the crystallographic structure shows of the topology of the iron−sulfur cluster (Figure 9). The cluster is buried within the protein, with no crystallographic waters in contact with cluster atoms. However, the solvent might have access to the cluster through a "window" located along the S1−S2 direction near the sulfur S2, which we have suggested to be hydrogen bonded with the peptide nitrogen of Leu-132.

A simple explanation of this observation can then be given in terms of a model considering the weak dipole−dipole interaction of the effective electron spin $S = {}^1/_2$ of the reduced cluster with coupled distant protons. To interpret the magnetic resonance data in conjunction with crystal structures, one needs to know the orientation of the **g**-tensor principal axes. For a qualitative consideration, the single-crystal EPR data from the reduced Rieske cluster in the bc_1 complex with stigmatellin allows us to suggest that the g_z and g_x axes are to a good approximation oriented along the S−S and Fe−Fe directions, respectively, and g_y is nearly normal to the cluster plane.[40] The modulation depth and intensity of the corresponding line in ESEEM spectra depend on the angle between the direction of the magnetic field and the vector connecting an electron and a nucleus. The ESEEM amplitude is close to zero for the angles close to 0° and 90° and increases for intermediate angles, reaching its maximum at 45°. For measurements performed at the edges of the EPR spectrum, when the magnetic field is directed along the g_z and g_x principal axes of the tensor, i.e., oriented closely to S−S and Fe−Fe directions, the vector directed toward proton(s) of solvent molecule located in the "window" would form angles close to 0° and 90°, respectively. For measurements in the central part of the EPR line many different orientations contribute to the HYSCORE spectra and some of them would have favorable angles that would lead to an increase of intensity from solvent molecules.

Conclusion

In this work we have reported the first application of 2D ESEEM to characterize the proton environment of a reduced [2Fe-2S] cluster, taking the ISP from *Rb. sphaeroides* as an example. The data provide the entrée to a number of new research initiatives that will allow a complete characterization of the local environment that determines the thermodynamic properties of this important center. In particular, the availability of high-resolution structures of the wild-type, and of a wide range of mutations that change those properties, will make possible both a validation of the spectroscopic approach, a synergistic enhancement of similar spectroscopic studies through ENDOR, and cross correlation with quantum-chemical simulations that model the geometry of this particular cluster in the reduced and oxidized states of the cluster.

Determination of the proton environment through pulsed X-band EPR addresses two major problems, which would be typical for similar studies of paramagnetic metal centers in other proteins. First is the large number of protons producing multiple overlapping lines in ENDOR or ESEEM spectra. Second is the lack of an effective general methodology for deconvolution of 1D ENDOR or ESEEM spectra that can separate the individual contributions from different protons. The most detailed proton ENDOR studies of [2Fe-2S] clusters, in which 20−25 orientation-selected spectra were considered, were based on an initial analysis of the three or four largest couplings, well separated in the spectra, usually assigned to the β-protons of the cysteines coordinating the Fe(III).[64,65] These couplings allowed a straightforward correlation to the same protons in different spectra. Simulation of the field or g-value dependences of these couplings was a major part of these studies, and provided principal values for the HF tensors, and the orientation of the principal axes in the coordinate system of the **g**-tensor. However, the distribution of unpaired spin density was a variable parameter in these simulations. The proton tensors obtained were correlated with crystallographic structures to establish the orientation of the **g**-tensor relative to the cluster molecular axes, and assignment of the tensor to particular β-protons near Fe(III). The significant overlap of the lines in the central part of the spectra, where contributions from more weakly coupled protons are found, prevented unambiguous construction of the orientation dependence of the couplings from these protons. The spectral contributions of these nonexchangeable and exchangeable protons were therefore estimated by using the X-ray structures.

In contrast to the ENDOR analysis, the orientation-selected 2D ESEEM spectra, and the protocols for analysis based on correlation of the resolved cross-peaks, allow one to obtain the principal values of the HF tensors directly from experimental spectra without regard to any simulation model. The tensors obtained from the resolved signals represent different groups of protons. On other hand, these data do not provide any information on orientation, because the influence of the **g**-tensor anisotropy on the proton frequencies is ignored.

The further development of this approach would be in combination with orientation-selected ENDOR. The HF tensors estimated from HYSCORE can help in the correlation of the peaks belonging to the same protons in different ENDOR spectra, and can be used in the simulation of the orientation dependence of the couplings, thus decreasing the number of variable parameters used in the fitting procedure. Such a combined approach might finally lead to an assignment to particular protons based on the information obtained on orientation.

Detailed information about bond lengths and angles is important in simulation of thermodynamic properties. Extension of our EPR studies to mutant strains is well in hand, and will provide similar data allowing identification of changes in the protein environment following specific mutation at four residues known to contribute to changes in thermodynamic properties. We also have in hand high-resolution structures of some dozen of these mutant strains (in collaboration with Prof. Satish Nair), and detailed mechanistic and thermodynamic studies to allow

development of a comprehensive picture of the physicochemical underpinnings of the functional parameters.

The approach developed here will be of particular interest in application to other similar proteins. Validation of the spectroscopic approach in the context of well-resolved structures provides a greater security in interpretation of data where either no structure or only a low-resolution structure is available. Potential improvements in the high-resolution EPR approach might involve the analysis of the deuterium lines in 1D and 2D ESEEM appearing after deuterium exchange, extension to ESEEM at Q-band, and to application of lower microwave frequencies such as S-band, where fields appropriate to a microwave frequency of ~3 GHz[81] bring into play different cancelation conditions that can be used to resolve ambiguities in data obtained at higher frequencies. These approaches will also be important where uncertainties exist in the oxidation state of the cluster in a crystallographic structure because of the possibility of radiolytic reduction during X-ray illumination, since the EPR approach explores a unique redox state.

Acknowledgment. This work is supported by National Institutes of Health Grants GM 35438 (to A.R.C.) and GM 62954 (to S.A.D.), Fogarty Grant PHS 1 RO3 TW 01495 (to A.R.C. and R.I.S.), and National Institutes of Health/National Center for Research Resources Grant S10-RR15878 for instrumentation.

Supporting Information Available: Characteristics of HYSCORE spectra from $I = {}^1/_2$ nuclei, cross-suppression effects in HYSCORE spectra, and assignment of signal 7. This material is available free of charge via the Internet at http://pubs.acs.org.

References and Notes

(1) Crofts, A. R.; Meinhardt, S. W.; Jones, A. K.; Snozzi, M. *Biochem. Biophys. Acta* **1983**, *723*, 202.
(2) Crofts, A. R.; Shinkarev, V. P.; Kolling, D. R.; Hong, S. *J. Biol. Chem.* **2003**, *278*, 36191.
(3) Crofts, A. R.; Guergova-Kuras, M.; Kuras, R.; Ugulava, N.; Li, J.; Hong, S. *Biochem. Biophys. Acta* **2000**, *1459*, 456.
(4) Hong, S.; Ugulava, N.; Guergova-Kuras, M.; Crofts, A. R. *J. Biol. Chem.* **1999**, *274*, 33931.
(5) Crofts, A. R.; Barquera, B.; Gennis, R. B.; Kuras, R.; Guergova-Kuras, M.; Berry, E. A. *Biochemistry* **1999**, *38*, 15807.
(6) Crofts, A. R.; Guergova-Kuras, M.; Huang, L.; Kuras, R.; Zhang, Z.; Berry, E. A. *Biochemistry* **1999**, *38*, 15791.
(7) Crofts, A. R.; Hong, S.; Ugulava, N.; Barquera, B.; Gennis, R.; Guergova-Kuras, M.; Berry, E. A. *Proc. Natl. Acad. Sci. U.S.A.* **1999**, *96*, 10021.
(8) Dikanov, S. A.; Samoilova, R. I.; Kolling, D. R.; Holland, J. T.; Crofts, A. R. *J. Biol. Chem.* **2004**, *279*, 15814.
(9) Kolling, D. R.; Samoilova, R. I.; Holland, J. T.; Berry, E. A.; Dikanov, S. A.; Crofts, A. R. *J. Biol. Chem.* **2003**, *278*, 39747.
(10) Zhang, Z.; Huang, L.; Shulmeister, V. M.; Chi, Y. I.; Kim, K. K.; Hung, L. W.; Crofts, A. R.; Berry, E. A.; Kim, S. H. *Nature* **1998**, *392*, 677.
(11) Crofts, A. R.; Berry, E. A. *Curr. Opin. Struct. Biol.* **1998**, *8*, 501.
(12) Izrailev, S.; Crofts, A. R.; Berry, E. A.; Schulten, K. *Biophys. J.* **1999**, *77*, 1753.
(13) Hunte, C.; Koepke, J.; Lange, C.; Rossmanith, T.; Michel, H. *Struct. Fold Des.* **2000**, *8*, 669.
(14) Crofts, A.; Guergova-Kuras, M.; Ugulava, N.; KurasR. Hong, S. In *Proceedings of the XIIth Congress of Photosynthesis Research*, Brisbane, Australia, 2002, p 6.
(15) Crofts, A. R.; Barquera, B.; Gennis, R. B.; Kuras, R.; Guergova-Kuras, M.; Berry, E. A. In *The Phototrophic Prokaryotes*; Peschek, G. A., Loeffelhardt, W., Schmetterer, G., Eds.; Plenum Publishing Corporation: New York, 1999; pp 229−239.
(16) Crofts, A. R. *Annu. Rev. Physiol.* **2004**, *66*, 689.
(17) Crofts, A. R. *Biochim. Biophys. Acta* **2004**, *1655*, 77.
(18) Osyczka, A.; Moser, C. C.; Daldal, F.; Dutton, P. L. *Nature* **2004**, *427*, 607.
(19) Crofts, A. R.; Hong, S.; Zhang, Z.; Berry, E. A. *Biochemistry* **1999**, *38*, 15827.
(20) Liebl, U.; Penzennec, S.; Riedel, A.; Kellner, E.; Nitschke, W. *J. Biol. Chem.* **1992**, *267*, 14068.
(21) Rich, P. R. *Biochim. Biophys. Acta* **1984**, *768*, 53.
(22) Link, T. A. *Adv. Inorg. Chem.* **1999**, *47*, 83.
(23) Zu, Y.; Couture, M. M.; Kolling, D. R.; Crofts, A. R.; Eltis, L. D.; Fee, J. A.; Hirst, J. *Biochemistry* **2003**, *42*, 12400.
(24) Hunsicker-Wang, L. M.; Heine, A.; Chen, Y.; Luna, E. P.; Todaro, T.; Zhang, Y. M.; Williams, P. A.; McRee, D. E.; Hirst, J.; Stout, C. D.; Fee, J. A. *Biochemistry* **2003**, *42*, 7303.
(25) Colbert, C. L.; Couture, M. M.; Eltis, L. D.; Bolin, J. T. *Structure* **2000**, *8*, 1267.
(26) Shinkarev, V. P.; Kolling, D. R.; Miller, T. J.; Crofts, A. R. *Biochemistry* **2002**, *41*, 14372.
(27) Cooley, J. W.; Roberts, A. G.; Bowman, M. K.; Kramer, D. M.; Daldal, F. *Biochemistry* **2004**, *43*, 2217.
(28) Darrouzet, E.; Valkova-Valchanova, M.; Daldal, F. *J. Biol. Chem.* **2002**, *277*, 3464.
(29) Iwata, S.; Lee, J. W.; Okada, K.; Lee, J. K.; Iwata, M.; Rasmussen, B.; Link, T. A.; Ramaswamy, S.; Jap, B. K. *Science* **1998**, *281*, 64.
(30) Berry, E. A.; Huang, L.-S.; Saechao, L. K.; Pon, N. G.; Valkova-Valchanova, M.; Daldal, F. *Photosynth. Res.* **2004**, *81*, 251.
(31) Ding, H.; Moser, C. C.; Robertson, D. E.; Tokito, M. K.; Daldal, F.; Dutton, P. L. *Biochemistry* **1995**, *34*, 15979.
(32) Ding, H.; Robertson, D. E.; Daldal, F.; Dutton, P. L. *Biochemistry* **1992**, *31*, 3144.
(33) Sharp, R.; Palmitessa, A.; Gibney, B.; White, J.; Moser, C.; Daldal, F.; Dutton, P. *Biochemistry* **1998**, *38*, 3440.
(34) Sharp, R. E.; Gibney, B. R.; Palmitessa, A.; White, J. L.; Dixon, J. A.; Moser, C. C.; Daldal, F.; Dutton, P. L. *Biochemistry* **1999**, *38*, 14973.
(35) Sharp, R. E.; Moser, C. C.; Gibney, B. R.; Dutton, P. L. *J. Bioenerg. Biomembr.* **1999**, *31*, 225.
(36) Sharp, R. E.; Palmitessa, A.; Gibney, B. R.; Moser, C. C.; Daldal, F.; Dutton, P. L. *FEBS Lett.* **1998**, *431*, 423.
(37) Sharp, R. E.; Palmitessa, A.; Gibney, B. R.; Daldal, F.; Moser, C. C.; Dutton, P. L. In *The Phototrophic Prokaryotes*; Kluwer Academic/Plenum Publishers: New York, 1999..
(38) Samoilova, R. I.; Kolling, D.; Uzawa, T.; Iwasaki, T.; Crofts, A. R.; Dikanov, S. A. *J. Biol. Chem.* **2002**, *277*, 4605.
(39) Shubin, A. A.; Dikanov, S. A. *Appl. Magn. Reson.* **2006**, *30*, 399.
(40) Bowman, M. K.; Berry, E. A.; Roberts, A. G.; Kramer, D. M. *Biochemistry* **2004**, *43*, 430.
(41) Iwasaki, T.; Kounosu, A.; Uzawa, T.; Samoilova, R. I.; Dikanov, S. A. *J. Am. Chem. Soc.* **2004**, *126*, 13902.
(42) Dikanov, S. A.; Shubin, A. A.; Kounosu, A.; Iwasaki, T.; Samoilova, R. I. *J. Biol. Inorg. Chem.* **2004**, *9*, 753.
(43) Dikanov, S. A.; Kolling, D. R. J.; Endeward, B.; Samoilova, R. I.; Prisner, Th. F.; Nair, S. K.; Crofts, A. R. *J. Biol. Chem.* **2006**, *281*, 27416.
(44) Iwasaki, T.; Kounosu, A.; Samoilova, R. I.; Dikanov, S. A. *J. Am. Chem. Soc.* **2006**, *128*, 2170.
(45) Iwasaki, T.; Kounosu, A.; Kolling, D. R. J.; Lhee, S.; Crofts, A. R.; Dikanov, S. A.; Uchiyama, T.; Kumasaka, T.; Ichikawa, H.; Kono, M.; Imai, T.; Urushiyama, A. *Protein Sci.* **2006**, *15*, 2019.
(46) Höfer, P.; Grupp, A.; Nebenfür, H.; Mehring, M. *Chem. Phys. Lett.* **1986**, *132*, 279.
(47) Dikanov, S. A.; Tyryshkin, A. M.; Bowman, M. K. *J. Magn. Reson.* **2000**, *144*, 228.
(48) Britt, R. D.; Sauer, K.; Klein, M. P.; Knaff, D. B.; Kriauciunas, A.; Yu, C. A.; Yu, L.; Malkin, R. *Biochemistry* **1991**, *30*, 1892.
(49) Shergill, J. K.; Cammack, R. *Biochim. Biophys. Acta* **1994**, *1185*, 35.
(50) Shergill, J. K.; Joannou, C. L.; Mason, J. R.; Cammack, R. *Biochemistry* **1995**, *34*, 16533.
(51) Dikanov, S. A.; Xun, L.; Karpiel, A. B.; Tyryshkin, A. M.; Bowman, M. K. *J. Am. Chem. Soc.* **1996**, *118*, 8408.
(52) Stoll, S.; Calle, C.; Mitrikas, G.; Schweiger, A. *J. Magn. Reson.* **2005**, *177*, 93–101.
(53) Dikanov, S. A.; Bowman, M. K. *J. Biol. Inorg. Chem.* **1998**, *3*, 18.
(54) Dikanov, S. A.; Bowman, M. K. *J. Magn. Reson. Ser. A* **1995**, *116*, 125.
(55) Rowan, L. G.; Hahn, E. L.; Mims, W. B. *Phys. Rev. A* **1965**, *137*, 61.
(56) Yap, L.-L.; Samoilova, R. I.; Gennis, R. B.; Dikanov, S. A. *J. Biol. Chem.* **2006**, *281*, 16879.
(57) Kolling, D. J.; Brunzelle, J. S.; Lhee, S.; Crofts, A. R.; Nair, S. K. *Structure* **2007**, *15*, 29.
(58) Khangulov, S.; Sivaraja, M.; Barynin, V. V.; Dismukes, G. C. *Biochemistry* **1993**, *32*, 4912.
(59) Fiege, R.; Zweygart, W.; Bittl, R.; Adir, N.; Renger, G.; Lubitz, W. *Photosyn. Res.* **1996**, *48*, 227.
(60) Randall, D. W.; Gelasco, A.; Caudle, M. T.; Pecoraro, V. L.; Britt, R. D. *J. Am. Chem. Soc.* **1997**, *119*, 4481.
(61) DeRose, V. J.; Liu, K. E.; Lippard, S. J.; Hoffman, B. M. *J. Am. Chem. Soc.* **1996**, *118*, 121.

(62) Willems, J.-P.; Lee, H.-L.; Burdi, D.; Doan, P. E.; Stubbe, J.; Hoffman, B. M. *J. Am. Chem. Soc.* **1997**, *119*, 9816.
(63) Mouesca, J.-M.; Noodleman, L.; Case, D. A.; Lamotte, B. *Inorg. Chem.* **1995**, *34*, 4347.
(64) Canne, C.; Ebelshäuser, M.; Gay, E.; Shergill, J. K.; Cammack, R.; Kappl, R.; Hüttermann, J. *J. Biol. Inorg. Chem.* **2000**, *5*, 514.
(65) Kappl, R.; Ebelshäuser, M.; Hannemann, F.; Bernhardt, R.; Hüttermann, J. *Appl. Magn. Reson.* **2006**, *30*, 427.
(66) Gurbiel, R. J.; Doan, P. E.; Gassner, G. T.; Macke, T. J.; Case, D. A.; Ohnishi, T.; Fee, J. A.; Ballow, D. P.; Hoffman, B. M. *Biochemistry* **1996**, *35*, 7834.
(67) Holz, R. C.; Small, F. J.; Ensign, S. A. *Biochemistry* **1997**, *36*, 14690.
(68) Xia, B.; Pikus, J. D.; Xia, W.; McClay, K.; Steffan, R. J.; Chae, Y. K.; Westler, W. M.; Markley, J. L.; Fox, B. G. *Biochemistry* **1999**, *38*, 727–739.
(69) Dugad, L. B.; La Mar, G. N.; Banci, L.; Bertini, I. *Biochemistry* **1990**, *29*, 2263.
(70) Chae, Y. K.; Xia, B.; Cheng, H.; Oh, B.-H.; Skjeldal, L.; Westler, W. M.; Markley, J. L. In *Nuclear magnetic resonance of paramagnetic macromolecules*; Kluwer: Dordrecht, The Netherlands, 1995; pp 297−317.
(71) Fukuyama, K.; Ueki, N.; Nakamura, M.; Tsukihara, T.; Matsubara, H. *J. Biochem. (Tokyo)* **1995**, *117*, 1017.
(72) Müller, A.; Müller, J. J.; Muller, Y. A.; Uhlmann, H.; Bernhardt, R.; Heinemann, U. *Structure* **1998**, *6*, 269–280.
(73) Iwata, S.; Saynovits, M.; Link, T. A.; Michel, H. *Structure* **1996**, *4*, 567.
(74) Mouesca, J.-M.; Rills, G.; Lamotte, B. *J. Am. Chem. Soc.* **1993**, *115*, 4714.
(75) Noodleman, L.; Chen, J.-L.; Case, D. A.; Giori, C.; Rius, G.; Mouesca, J.-M.; Lamotte, B. In *Nuclear Magnetic Resonance of Paramagnetic Macromolecules*; La Mar, G. N., Ed.; Kluwer: Dordrecht, The Netherlands, pp. 339−367, 1995.
(76) Moriaud, F.; Gambarelli, S.; Lamotte, B.; Mouesca, J.-M. *J. Phys. Chem. B* **2001**, *105*, 9631.
(77) Kappl, R.; Ciurli, S.; Luchinat, C.; Hüttermann., J. *J. Am. Chem. Soc.* **1999**, *121*, 1925.
(78) Ugulava, N. B.; Crofts, A. R. *FEBS Lett.* **1998**, *440*, 409.
(79) Cammack, R.; Gay, E.; Shergill, J. K. *Coord. Chem. Rev.* **1999**, *190−192*, 1003.
(80) Noodleman, L.; Peng, C. Y.; Case, D. A.; Mouesca, J.-M. *Coord. Chem. Rev.* **1995**, *144*, 199.
(81) Astashkin, A. V.; Raitsimring, A. M.; Walker, F. A. *Chem. Phys. Lett.* **1999**, *306*, 9.

JP806789X